

A Compressive Sensing Data Acquisition and Imaging Method for Stepped Frequency GPRs

Ali Cafer Gurbuz, *Member, IEEE*, James H. McClellan, *Fellow, IEEE*, and Waymond R. Scott, *Fellow, IEEE*

Abstract—A novel data acquisition and imaging method is presented for stepped-frequency continuous-wave ground penetrating radars (SFCW GPRs). It is shown that if the target space is sparse, i.e., a small number of point like targets, it is enough to make measurements at only a small number of random frequencies to construct an image of the target space by solving a convex optimization problem which enforces sparsity through ℓ_1 minimization. This measurement strategy greatly reduces the data acquisition time at the expense of higher computational costs. Imaging results for both simulated and experimental GPR data exhibit less clutter than the standard migration methods and are robust to noise and random spatial sampling. The images also have increased resolution where closely spaced targets that cannot be resolved by the standard migration methods can be resolved by the proposed method.

Index Terms—Compressive sensing, ℓ_1 minimization, ground penetrating radar (GPR), sparsity, stepped frequency systems, subsurface imaging.

I. INTRODUCTION

GROUND Penetrating Radar (GPR) [1] is an important remote sensing tool in a wide variety of areas such as civil engineering [2], landmine detection [3]–[5], archeological investigations [6] and environmental applications [7]. Traditional GPRs image the subsurface by transmitting short electromagnetic (EM) pulses and processing the reflections due to permittivity discontinuities in the ground.

The traditional impulse GPR is a common type of GPR due to its simple design and low cost [8]. Another type of GPR that is becoming increasingly popular is the stepped-frequency continuous-wave (SFCW) GPR [9]–[12]. In [5], [13]–[15] SFCW GPR is used to image buried landmines and objects. A stepped-frequency signal probes the environment with a discrete set of frequencies, and has several advantages over an impulse GPR. The main advantage is greater measurement accuracy, because it is much easier to synthesize a pure tone at a given frequency than to measure a time delay, i.e., the accuracy with which the

frequencies are set in the SFCW GPR is much greater than the measurement times used in an impulse GPR. The SFCW GPR also has a greater dynamic range and lower noise because it can transmit higher power and uses a very narrow IF bandwidth. The filtering used can greatly reduce the interference from nearby transmitters such as RF communication links. A SFCW GPR can also be programmed to skip over a defined frequency band, so that it will not interfere with instruments on sensitive frequency bands. The operating frequency range can also be adjusted for targets at different depths by using the low-frequency range for relatively deep targets, and higher frequencies for shallow objects [10]. Frequency steps can also be selected randomly as in [12].

Although SFCW GPRs have very good properties, they are not used widely in commercial systems [16]–[18]. One important reason for this is long data acquisition times. The time taken at each scan position per frequency depends on several issues, such as the switching time for the sources, two-way travel time to reach targets at a chosen maximum range, and the time for the receiver to build up sufficient SNR. For example, in [17] it is reported that an SFCW GPR can take measurements at a rate of 25 per second. The system operates in the band 1–3 GHz and takes 400 measurements at each scan position. With this measurement rate, the system can be scanned at a speed of 1.8 kph with a 2-cm spatial increment which is too slow for some applications. GPRs with higher acquisition rates can and have been built, but users have applications which need ever increasing scanning speeds. For such applications, it is important to increase the speed of the system without degrading its performance.

The total subsurface frequency response formed from a combination of responses from all reflectors within the medium can be inverted using various imaging algorithms. One type transforms the measured frequency-domain data to time-domain signals by applying an IFFT to each A-Scan measurement, followed by time-domain backprojection (TDBP) [4], [19] to create an image of the target space. Frequency domain imaging algorithms [20]–[22] directly use the SFCW data to create the target space image. These algorithms basically perform matched filtering with the impulse response of the data acquisition process to form the images.

We propose a novel data acquisition and imaging algorithm for SFCW GPRs based on random selection of the measurement frequencies which significantly reduces the data acquisition time and also creates less cluttered target space images when compared to time/frequency domain BP. The proposed method depends on a basic assumption of spatial sparsity. Generally potential targets cover a small part of the total subsurface volume to be imaged. Thus, a basic *a priori* information

Manuscript received May 13, 2008; accepted January 27, 2009. First published February 24, 2009; current version published June 17, 2009. The associate editor coordinating the review of this paper and approving it for publication was Prof. Alfred Hanssen. This work was supported by an ARO-MURI Grant: “Multi-Modal Inverse Scattering for Detection and Classification of General Concealed Targets” under contract number DAAD19-02-1-0252.

A. C. Gurbuz is with the Department of Electric and Electronics Engineering, TOBB University of Economics and Technology, Ankara, Turkey (e-mail: alicafer@ieee.org).

J. H. McClellan and W. R. Scott are with the School of Electrical and Computer Engineering, Georgia Institute of Technology, Atlanta, GA 30332 USA (e-mail: jim.mcclellan@ece.gatech.edu; waymond.scott@ece.gatech.edu).

Color versions of one or more of the figures in this paper are available online at <http://ieeexplore.ieee.org>.

Digital Object Identifier 10.1109/TSP.2009.2016270

about the target space is its spatial sparsity, which is not exploited by the standard imaging methods. The spatial sparsity indicates that the number of targets is much less than the total number of spatial positions. The sparsity property of signals has found many interesting applications including image reconstruction [23], medical imaging [24], radar imaging [25], blind source separation [26], shape detection [27]. Recent results in the theory of compressive sensing (CS) [28]–[30] show how a sparsely representable signal can be reconstructed when sampled with a very small number of measurements. CS takes non-traditional linear measurements, $\mathbf{y} = \Phi \mathbf{x}$, in the form of randomized projections. A signal \mathbf{x} , which has a sparse representation in a transform domain Ψ , as $\mathbf{x} = \Psi \mathbf{s}$ can be reconstructed from $M = C(\mu^2(\Phi, \Psi) \log N) Q$ compressive measurement exactly with high probability by solving a convex ℓ_1 optimization problem of the following form:

$$\min \|\mathbf{s}\|_1, \text{ subject to } \mathbf{y} = \Phi \Psi \mathbf{s} \quad (1)$$

which can be solved efficiently with linear programming.

We apply ideas from CS to the problem of GPR subsurface imaging by formulating the imaging problem as a dictionary selection problem. The dictionary entries are produced by discretizing the target space, and synthesizing the GPR frequency model data for each discrete spatial position. Recently, there has been great interest in representing signals as a superposition of elements from an overcomplete dictionary, and many methods have been developed to extract an *optimal* representation in terms of the given dictionary elements; this kind of search is called *Basis Pursuit* [31], [32]. The assumptions made here are that the targets are point-like reflectors at discrete locations, the targets do not interact so superposition is valid, and the wave propagation obeys ray theory. The reason we use a point target reflectivity model is that the received data can be easily calculated for a point target. The point-like target assumption is not crucial; other models can be used as long as the received data can be calculated for the assumed target model. The sparsity assumption is also not limited to point targets; other models can be used as long as the targets are sparse or compressible in some transform domain.

Instead of measuring all the frequencies, only a random subset of frequencies is measured and a convex optimization problem similar to (1) which takes into account noisy measurements is solved. This shifts most of the load from the data acquisition to the signal processing. The proposed compressive imaging method is significantly different from the standard imaging approaches of TDBP [4], [19], or frequency-domain migration [20]–[22] algorithms which require a high number of uniform frequency measurements. Also less cluttered images are formed since the formulation forces sparse results. In addition to random sampling in the frequency domain, the spatial aperture can be sampled randomly [33] without degrading the created image significantly. Random spatial sampling gives additional savings in the data acquisition time. Another important property of the proposed method is its ability to resolve closely spaced targets like observed in [34], [35] that cannot be resolved by the standard migration methods. The proposed method doesn't perform matched filtering which has

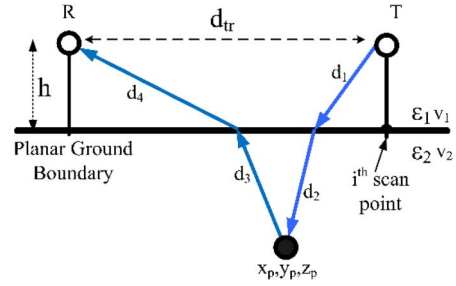


Fig. 1. GPR measurement setup showing a bistatic scenario.

a resolution limit; instead, it tries to explain the measurements using several elements from a dictionary of measurements.

The organization of the paper is as follows. Section II describes the compressive imaging algorithm. Selection of the algorithm parameters is explained in Section III. Section IV presents results for simulated and experimental SFCW GPR data along with a performance analysis in varying conditions. Conclusions are drawn in Section V.

II. THEORY FOR COMPRESSIVE IMAGING

As the SFCW GPR scans a region, at each scan position it transmits L continuous sinusoidal signals, sequentially changing the frequency. The transmitted signal for frequency ℓ , $\omega_\ell = 2\pi(f_0 + \ell\Delta f)$, can be written as

$$E_T(\ell, t) = A e^{-j2\pi(f_0 + \ell\Delta f)t} = A e^{-j\omega_\ell t} \quad (2)$$

where $\ell = 0, 1, 2, \dots, L-1$ with L being the total number of frequency steps, Δf the frequency step interval, and f_0 the initial frequency. A is the strength of the transmitted signal. In the case of a mono-static GPR antenna in a homogeneous medium with a single target at distance R , the received signal can be written as a time-delayed version of the transmitted signal [8] in (2)

$$E_R(\ell, t) = \frac{A}{S(R)} \sigma e^{-j\omega_\ell(t-2R/c)} = \frac{A}{S(R)} \sigma e^{j(2kR - \omega_\ell t)}. \quad (3)$$

In (3) σ is the reflection coefficient of the target, k is the propagation constant, and $S(R)$ is the spreading function explaining the decay of the signal and c is the wave propagation velocity in the medium.

In the two-layer scenario shown in Fig. 1, a bistatic GPR sensor is situated at a known height from the ground/air interface with buried targets. This is a more general and realistic case, but it is much harder to figure out the time delay. According to the ray theory view of electromagnetic (EM) wave propagation, the transmitted signal follows the path in Fig. 1. At the boundary between two different media (such as air and soil) the propagation direction changes according to Snell's law, but exact calculation of the refraction points requires the solution of a 4th degree polynomial. Several approximations are available [36]. After finding the refraction points, the distances $d_{1:4}$ in Fig. 1 can be calculated. The received signal for a single target at position p when the GPR is at scan position i can be written as

$$E_R(\ell, t, p, i) = \alpha(p) e^{j(k_1(d_1+d_4) + k_2(d_2+d_3) - \omega_\ell t)} \quad (4)$$

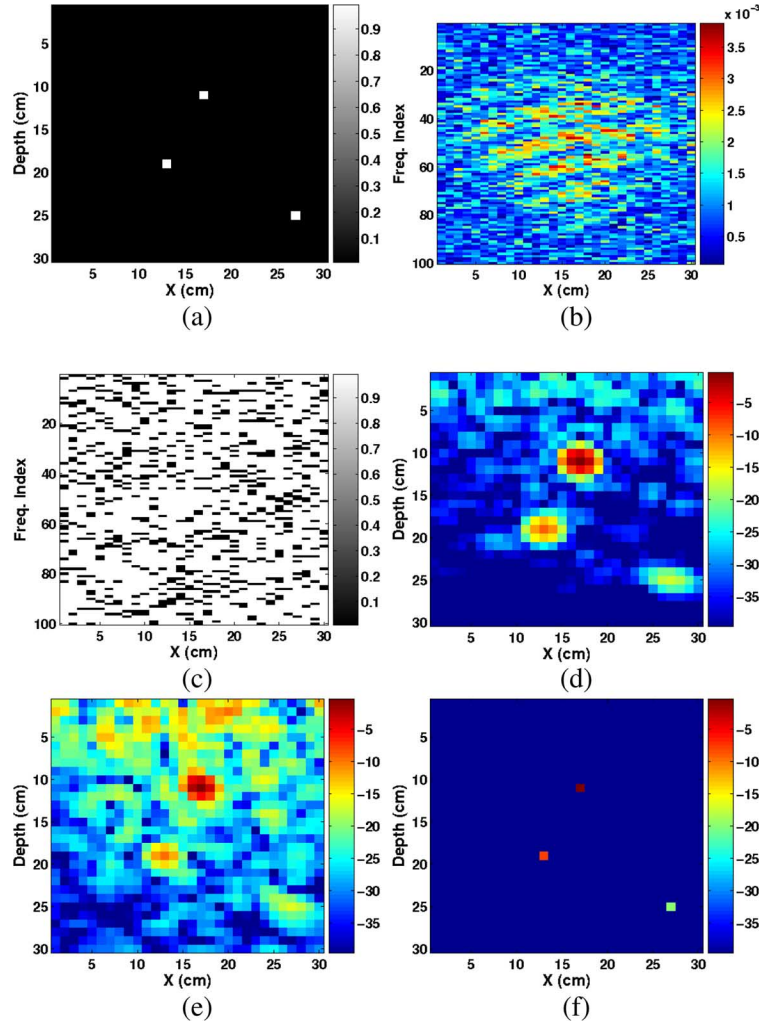


Fig. 2. (a) Target space. (b) Noisy space-frequency domain target space response at SNR = 10 dB for 30 scan positions. (c) Black points indicate the randomly measured frequencies when 20% of the total frequencies are used. (d) Frequency domain BP image using all the space-frequency data from (b). (e) Frequency domain BP method using only the randomly selected 20%. (f) Solution obtained with the CS method using (12).

where the distances depend on p and i ; $\alpha(p) = A\sigma/S(R(p))$, and k_1 and k_2 are the propagation constants in air and soil, respectively. So the received signal (4) can also be written in terms of the total time delay $\tau_i(p) = (d_1 + d_4)/v_1 + (d_2 + d_3)/v_2$, where v_1 and v_2 are the propagation velocities in air and soil.

To incorporate prior information about sparsity we must relate the measurements linearly to the spatial domain image as

$$\mathbf{d}(u_x, u_y, f) = \Psi \boldsymbol{\pi}_T(x, y, z) \quad (5)$$

where $\boldsymbol{\pi}_T(x, y, z)$ is the target space, $\mathbf{d}(u_x, u_y, f)$ are the space-frequency measurements, and Ψ is the operator defining the transform between the two spaces. In practice, we have a discrete version of the forward model (5) in which a sampled $\boldsymbol{\pi}_T$ is related to the observed discrete (noisy) frequency data through a linear discrete operator, i.e., a matrix Ψ .

A. Creating A Dictionary Matrix for GPR Data

To create the forward model Ψ , the target space $\boldsymbol{\pi}_T$ which lies in the product space $[x_i, x_f] \times [y_i, y_f] \times [z_i, z_f]$ must be discretized. Here, (x_i, y_i, z_i) and (x_f, y_f, z_f) denote the initial and final positions of the target space to be imaged along each

axis. Discretization generates a finite set of N target points $\mathcal{B} = \{\boldsymbol{\pi}_1, \boldsymbol{\pi}_2, \dots, \boldsymbol{\pi}_N\}$, where each $\boldsymbol{\pi}_j$ is a 3-D vector $[x_j; y_j; z_j]$. For any discrete target position the received frequency data for each frequency step and each scan position can be calculated using (4) with $\alpha(p) = 1$. For example, when the GPR is at the i th scan position, the j th column of Ψ_i which corresponds to a target at $\boldsymbol{\pi}_j$ can be written as

$$[\Psi_i]_j = \exp[-j\boldsymbol{\omega}(t - \tau_i(\boldsymbol{\pi}_j))] \quad (6)$$

where $\boldsymbol{\omega}$ is the vector of L frequencies. Repeating (6) for each discrete target position creates the dictionary Ψ_i of size $L \times N$ when the GPR is at the i th scan position.

The frequency response measurements at the i th scan position for P targets can be written as

$$\zeta_i(\boldsymbol{\omega}) = \sum_{k=1}^P \mathbf{b}(k) \exp[-j\boldsymbol{\omega}(t - \tau_i(\boldsymbol{\pi}_k))] \quad (7)$$

assuming that the targets do not interact, i.e., superposition is valid. In terms of the dictionary matrix, we write (7) as

$$\zeta_i(\boldsymbol{\omega}) = \Psi_i \mathbf{b} \quad (8)$$

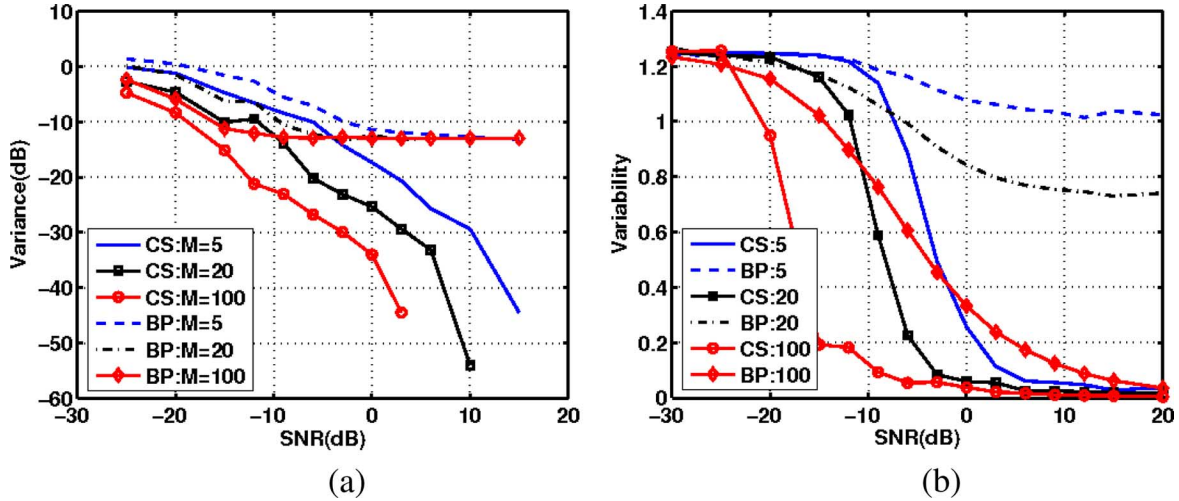


Fig. 3. (a) Target position variance versus SNR. (b) Variability of the created images versus SNR. Comparison between variances of BP and the CS method. M is the number of frequencies used.

where \mathbf{b} is a weighted indicator vector defining the target space, i.e., if there is a target at π_j , the value of the j th element of \mathbf{b} should be $A\sigma_j/S(R)$, otherwise, it is zero. Our goal is to find \mathbf{b} which is actually an “image” of the medium. We assume that $S(R)$ is unknown and include it in the estimation of \mathbf{b} ; but if $S(R)$ were known it could be included *a priori*.

B. Random Frequency Sampling

Standard SFCW GPRs measure at a fixed set of L frequencies for each scan position, hence the dimension of ζ_i is $L \times 1$. We propose a new data acquisition model based on compressive sampling (CS) [28]–[30] which would require many fewer samples to construct the target space image \mathbf{b} , if the target space is sparse. In the spirit of CS, a very small number of “random” measurements carry enough information to completely represent the signal. Thus, we measure at a random subset of M frequencies for each scan position. In matrix form the new measurements β_i can be written as

$$\beta_i = \Phi_i \zeta_i = \Phi_i \Psi_i \mathbf{b} \quad (9)$$

where Φ_i is an $M \times L$ measurement matrix constructed by randomly selecting M rows of an $L \times L$ identity matrix, which amounts to measuring random frequency points at the i th scan position. This reduces the data acquisition time by a factor of L/M for SFCW GPRs. Note that Φ_i which defines the measurements might be different for each scan position. The effects of selecting the same or a changing Φ_i for each scan position will be discussed in Section IV.

C. Compressive GPR Imaging

For imaging we use K scan positions and form a “super problem” with the composite matrices $\Psi = [\Psi_1^T, \dots, \Psi_K^T]^T$, and $\Phi = \text{diag}\{\Phi_1, \dots, \Phi_K\}$, and the measurements $\beta = [\beta_1^T, \dots, \beta_K^T]^T$. The result of the CS theory is that the target space indicator vector \mathbf{b} can be recovered exactly (with overwhelming probability) if the number of measurements MK is $\mathcal{O}(Q(\mu^2(\Phi, \Psi) \log N))$ [29], where Q is the

number of sparse targets and $\mu(\Phi, \Psi)$ is the coherence between Φ and Ψ [37]. The recovery of \mathbf{b} is done by solving a constrained ℓ_1 minimization problem

$$\hat{\mathbf{b}} = \text{argmin} \|\mathbf{b}\|_1 \text{ s.t. } \beta = \Phi \Psi \mathbf{b}. \quad (10)$$

The equality constraint in (10) is only valid for the noiseless case. If the GPR signal is noisy, then the measurements β_i at the i th scan position have the following form:

$$\beta_i = \Phi_i \zeta_i = \Phi_i \Psi_i \mathbf{b} + \mathbf{u}_i \quad (11)$$

where $\mathbf{u}_i = \Phi_i \mathbf{n}_i \sim \mathcal{N}(0, \sigma^2)$ and \mathbf{n}_i is the concatenation of the noise samples at scan position i , assumed to be $\mathcal{N}(0, \sigma_n^2)$. Since Φ_i is deterministic, we have $\sigma^2 = \left(\sum_{n=1}^{N_t} \phi_{imn}^2 \right) \sigma_n^2$. Hence, if we constrain the norm of the ϕ_{imn} vectors to be one, then $\sigma^2 = \sigma_n^2$.

It is shown in [38]–[41] that a stable recovery of the sparsity pattern vector \mathbf{b} is possible by solving a modified convex optimization problem, called the Dantzig Selector [39]

$$\hat{\mathbf{b}} = \text{arg min} \|\mathbf{b}\|_1 \text{ s.t. } \|\mathbf{A}^T(\beta - \mathbf{A}\mathbf{b})\|_\infty < \epsilon_1 \quad (12)$$

where $\mathbf{A} = \Phi \Psi$. Another possible solution comes from constraining the ℓ_2 -norm of the measurement error

$$\min \|\mathbf{b}\|_1 \text{ s.t. } \|\beta - \mathbf{A}\mathbf{b}\|_2 < \epsilon_2. \quad (13)$$

The target space images can be created using (12) or (13), but the ℓ_1 minimization in (12) is a linear program and easier to implement than (13) which is a second-order cone program [42]. The optimization problems in (10), (12), and (13) all minimize convex functionals, so a global optimum is guaranteed.

The convex optimization programs use interior point methods that iterate Newton’s method. For optimizing (12) or (13), the cost is $\mathcal{O}(N^3)$ with the observation that the number of iterations typically stays quite low, almost independent of the size of the problem [42], [43]. A theoretical worst case bound on

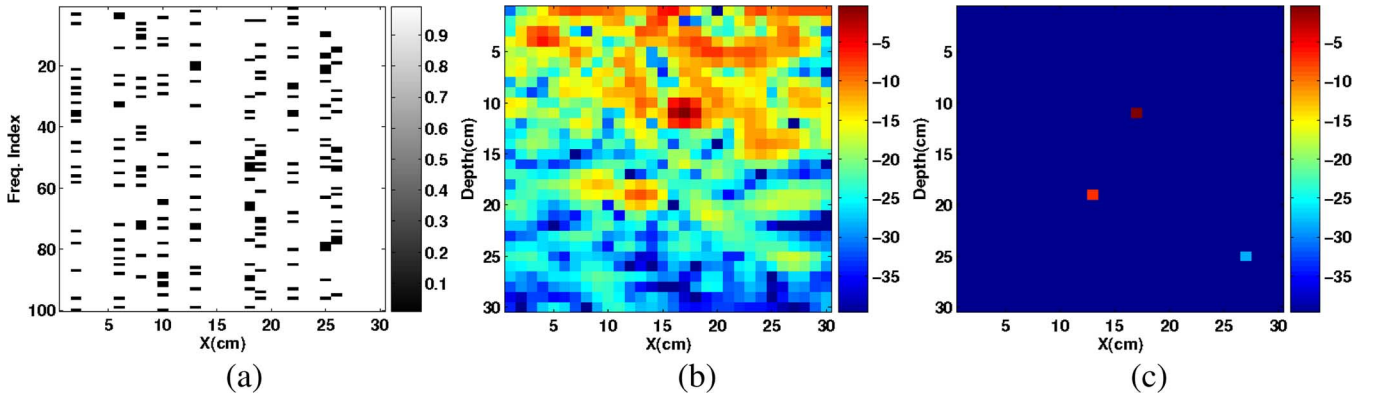


Fig. 4. (a) Space-frequency domain selection during the GPR data acquisition process at randomly sampled spatial scan positions. (b) Target space image with frequency domain BP. (c) Target space image with the CS method.

the number of iterations is given as $\mathcal{O}(\sqrt{N})$ [43]. The computational complexity is higher than that of BP, which has a complexity of $\mathcal{O}(NL)$ where L is the total number of frequency steps used. However, the benefit is generality, low number of measurements and lower data acquisition times, lower cluttered images, and increased resolution.

III. SELECTION OF ALGORITHM PARAMETERS

An important part of the proposed subsurface imaging system is the selection of two algorithm parameters: the spatial grid density, N , and the regularization parameter, ϵ_1 in (12) or ϵ_2 in (13), that controls the tradeoff between the sparsity of the solution and the closeness of the solution to the data.

Since discrete spatial grid positions are used to create the sparsity dictionary, the estimates of the target locations are confined to that grid. Increasing N makes the grid finer, but it also increases the algorithm complexity. Our method is suitable for multiresolution grid refinement. Initially a coarse grid might be used to obtain approximate knowledge of possible target locations. Later, the grid can be refined in regions where better precision is required. Making the initial grid too rough might introduce substantial bias into the estimates. Our results indicate that using a 0.5–1 cm depth spacing usually suffices.

Selecting a proper regularization parameter ϵ is very important. If ϵ is not set properly (12) either will not fully reconstruct the sparsity pattern vector and miss some targets (underfitting), or try to explain a significant portion of the noise by introducing spurious peaks. When the noise statistics of the data are known, a “good” choice of ϵ can be made. For example, with additive $\mathcal{N}(0, \sigma^2)$ noise, selecting $\epsilon = \sqrt{2 \log N} \sigma$ makes the true \mathbf{b} feasible with high probability [39].

In most cases, the noise statistics are unknown and need to be estimated. We propose an automatic method for selecting the regularization parameter based on cross-validation (CV) [44] that does not require any knowledge or estimate of noise statistics. The method depends on separating the measurements into two sets: the estimation set and the CV set. The CS imaging method is applied to the estimation set with an initial selection of ϵ , and the method’s result is tested on the CV set. As the algorithm iterates the prediction performance in the CV set increases. When the method starts to overfit the estimation data

TABLE I
VARIABILITY FOR REDUCED NUMBER OF SPATIAL SAMPLES

Reduced Spatial Sampling Test					
# of Apertures		30	20	10	6
Case 1	CS	0.020	0.048	0.083	0.167
	BP	0.745	0.868	0.976	1.072
Case 2	CS	0.020	0.040	0.083	0.135
	BP	0.745	0.778	0.801	0.824

set, i.e., estimating the noise, performance in the CV set decreases. Further decrease in ϵ is not beneficial and the algorithm should be terminated.

The CV based algorithm consists of the following steps:

- i) **Initialization:** Set $\epsilon = \alpha \|\mathbf{A}_E^T \boldsymbol{\beta}_E\|_\infty$, $\hat{\mathbf{b}} = 0$ and $i = 1$. An initial ϵ that prevents the method from overfitting the data can be selected by setting $\alpha = 0.99$. Note that for $\alpha > 1$, automatically $\hat{\mathbf{b}} = 0$ is the minimum ℓ_1 norm solution.
- ii) **Estimation:** Apply (12) to get an estimate of target locations $\hat{\mathbf{b}}^{(i)}$ using \mathbf{A}_E
- iii) **Cross-Validation:** if $\|\mathbf{A}_{CV}^T (\boldsymbol{\beta}_{CV} - \mathbf{A}_{CV} \hat{\mathbf{b}}^{(i)})\|_\infty < \epsilon$ then set $\epsilon = \|\mathbf{A}_{CV}^T (\boldsymbol{\beta}_{CV} - \mathbf{A}_{CV} \hat{\mathbf{b}}^{(i)})\|_\infty$, else terminate the algorithm
- iv) **Iteration:** Increase i by 1 and iterate from Step (ii).

IV. RESULTS

In this section, several simulated and experimental data results for the CS method are presented. First, to illustrate the random frequency sampling idea we test with a 2-D homogeneous target space of size 30 cm \times 30 cm containing three randomly placed point targets. A bistatic antenna with a 5 cm transmitter-receiver spacing at a height of 10 cm collects frequency domain measurements at frequencies from 100 MHz to 10 GHz with 100-MHz frequency steps. Thus, at each scan position the GPR collects 100 frequency measurements. The true target space image and the noisy space-frequency domain measurements are shown in Fig. 2(a) and (b). For the CS method instead of measuring all 100 frequencies, we only use a random subset of 20 frequencies at each scan

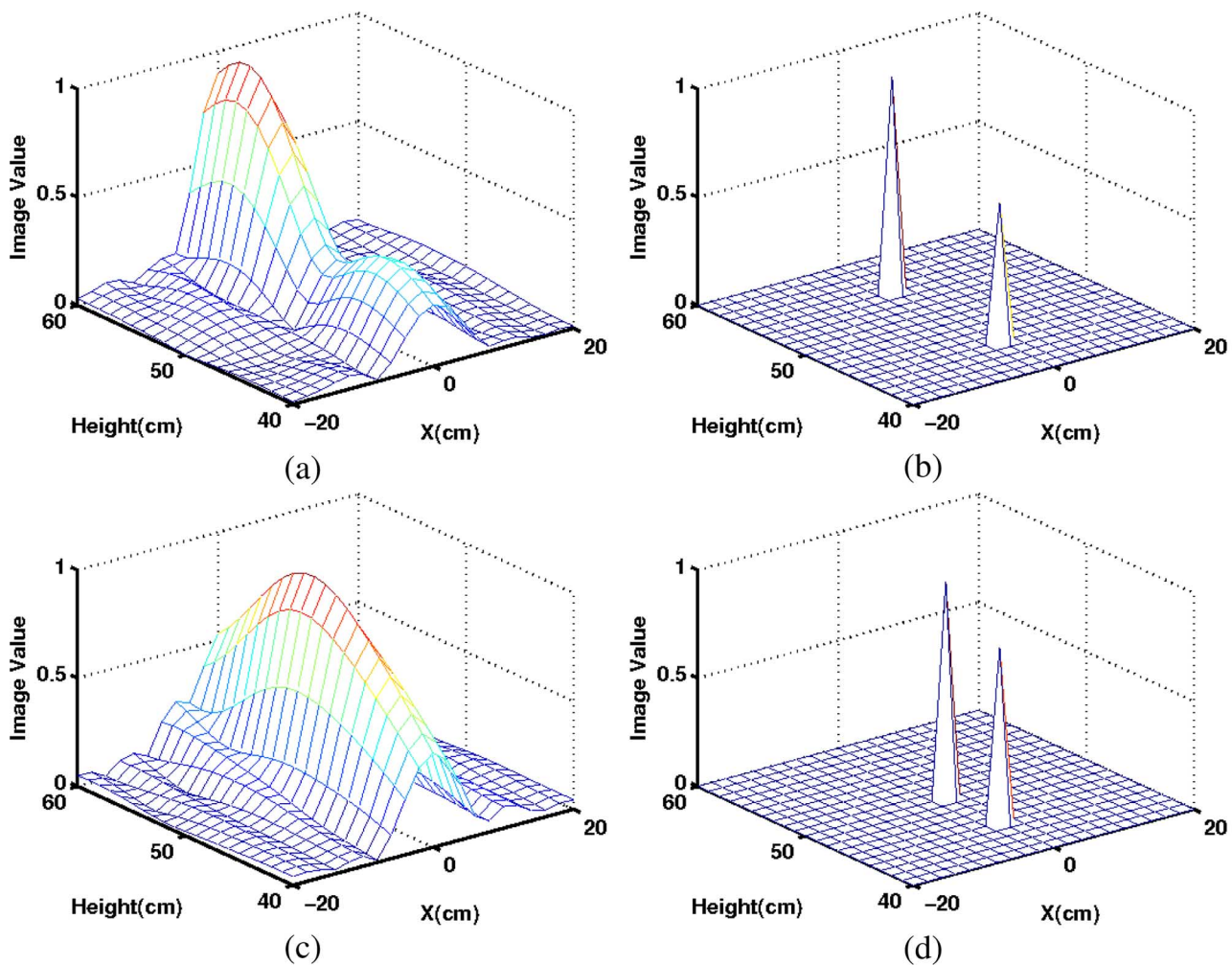


Fig. 5. Increased resolution property results: (a), (b) BP and CS images, respectively, when source separation is 10 cm. (c), (d) BP and CS images respectively for a source separation of 5 cm.

position. If we had measured all the space-frequency domain data and applied frequency domain BP, we would obtain the image shown in Fig. 2(d). The three targets can be seen clearly with small “blobs” around the correct target position. If we apply frequency domain BP to the randomly selected data, the resulting target space image is severely degraded as shown in Fig. 2(e). For the proposed CS method solving (12) with the randomly selected data generates the target space image shown in Fig. 2(f). For the numerical solution of (12) a convex optimization package called CVX [45] was used. The CS method finds the correct target positions with less clutter since the convex optimization program forces sparse solutions. All the target space images in Fig. 2(d)–(f) are normalized to their own maxima and are shown on the same 40-dB scale. As seen from the results while using a small number of frequencies, the CS method could generate a less cluttered image that is better than the BP method using all the frequency data.

As part of the testing, the target space image was formed 100 times by selecting an independent random measurement matrix at each time and applying the CS algorithm. It is observed that the algorithm introduces no bias to the target position estimates. Likewise, any random subset of frequencies works equally well as long as it contains more than the minimal number of mea-

surements. Note that the minimal required number of frequency measurements increases linearly with the number of reflectors in the image. Next, the performance of the algorithm in varying noise levels and the effect of using a different number of frequencies are discussed.

A. Performance in Noise

To analyze the impact of noise level on the estimated target positions and the image quality two simulations were done. First, with frequency domain GPR data for a single point target SNRs from -25 dB to 15 dB are tested with 50 different trials using additive CWGN at each SNR level. The target space is constructed via the CS algorithm using (12), and via BP with the random set frequency measurements at each scan position. For each SNR level, the variance of the estimated target locations is calculated and plotted in Fig. 3(a) for BP and the CS method.¹

It can be observed that the CS method using the same number of frequency measurements has smaller variances than the BP method. At high SNRs, the variance of BP does not change

¹To obtain the plot in Fig. 3(a) we used a grid size of 0.01 cm to get estimates not limited to a coarse grid.

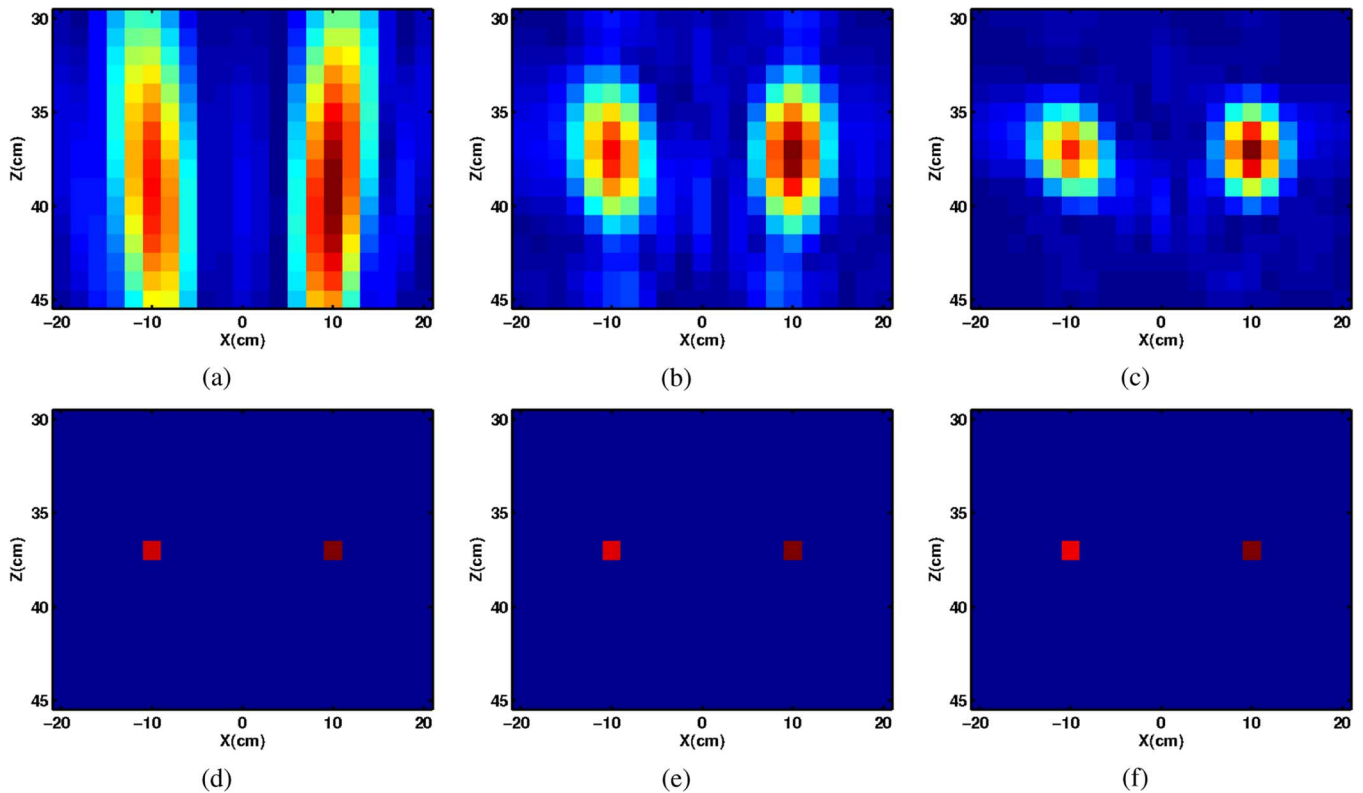


Fig. 6. Effect of bandwidth on the target space image created by both BP and the new CS method. (a), (b), and (c) are target space images created by BP at bandwidths of 1[3.5–4.5], 3[2.5–5.5] and 7[0.5–7.5] GHz, respectively. (d), (e), and (f) are target space images created by CS at bandwidths of 1, 3 and 7 GHz, respectively.

too much because BP reaches its resolution limit. The CS method provides much lower variances indicating increased resolution, which has also been observed in similar sparse signal reconstruction applications [46], [47]. We discuss this further in Section IV-C.

Second, we looked into the effect of noise on image quality and consistency. For this test, frequency GPR data is generated for three random point targets and corrupted with additive CWGN. After 50 trials, Fig. 3(b) shows the normalized variability of the images versus SNR level. Smaller image variability is an indication of both a correctly reconstructed and a sparse image. The CS method has much lower image variability than BP using the same number of measurements. This is because the CS method favors sparse solutions. This also indicates that the CS method is more robust compared to BP when the frequency measurements are selected at random.

B. Random Spatial Sampling

A joint convex optimization problem using frequency measurements from different scan positions is solved in (12) to create the target space image. The measured scan positions can be selected at random to reduce the number required for correct target space reconstruction. In Fig. 2, 20 frequency measurements at 30 scan positions were used. In this example, the same data set is used, but now 20 random frequencies are measured at only 10 randomly selected scan positions out of the 30. The measured space-frequency points are shown in Fig. 4(a). It can be observed that while reducing spatial samples highly

degrades the BP image, the CS method could still generate an image comparable to Fig. 2(f) with all the scan positions.

To better compare the effect of reduced random spatial sampling on both the CS method and BP, a Monte Carlo simulation was performed. Noisy GPR data for three point targets were generated for 30 scan positions with SNR = 10 dB. The target space is constructed using a subset of the random frequency measurements while varying the number of scan positions from 6 to 30. A subset of scan positions is randomly selected and the target space is reconstructed with (12) using only the measurements from the selected scan positions. This procedure is repeated 100 times with random aperture selections. Two cases are tested. In Case 1, $M = 20$ out of 100 frequencies are measured at the selected scan positions, for a total of 600 measurements when all 30 scan positions are used. In Case 2, the total number of measurements is kept at 600, i.e., when 15 scan positions are used $M = 40$ in Case 2, but Case 1 still uses $M = 20$. Table I shows the normalized image variability versus the number of scan positions, for both the CS method and BP. It can be observed from Table I that decreasing the number of apertures increases the variability of the target space image for both algorithms, even when the total number of measurements is fixed (Case 2). But the new CS method has a much lower variability than the BP method using the same measurements. Thus the CS method is more robust to the random selection of frequencies or scan positions. In comparing Cases 1 and 2, more measurements at each scan position won't decrease the variability for CS significantly, but additional measurements will reduce the variability for BP.

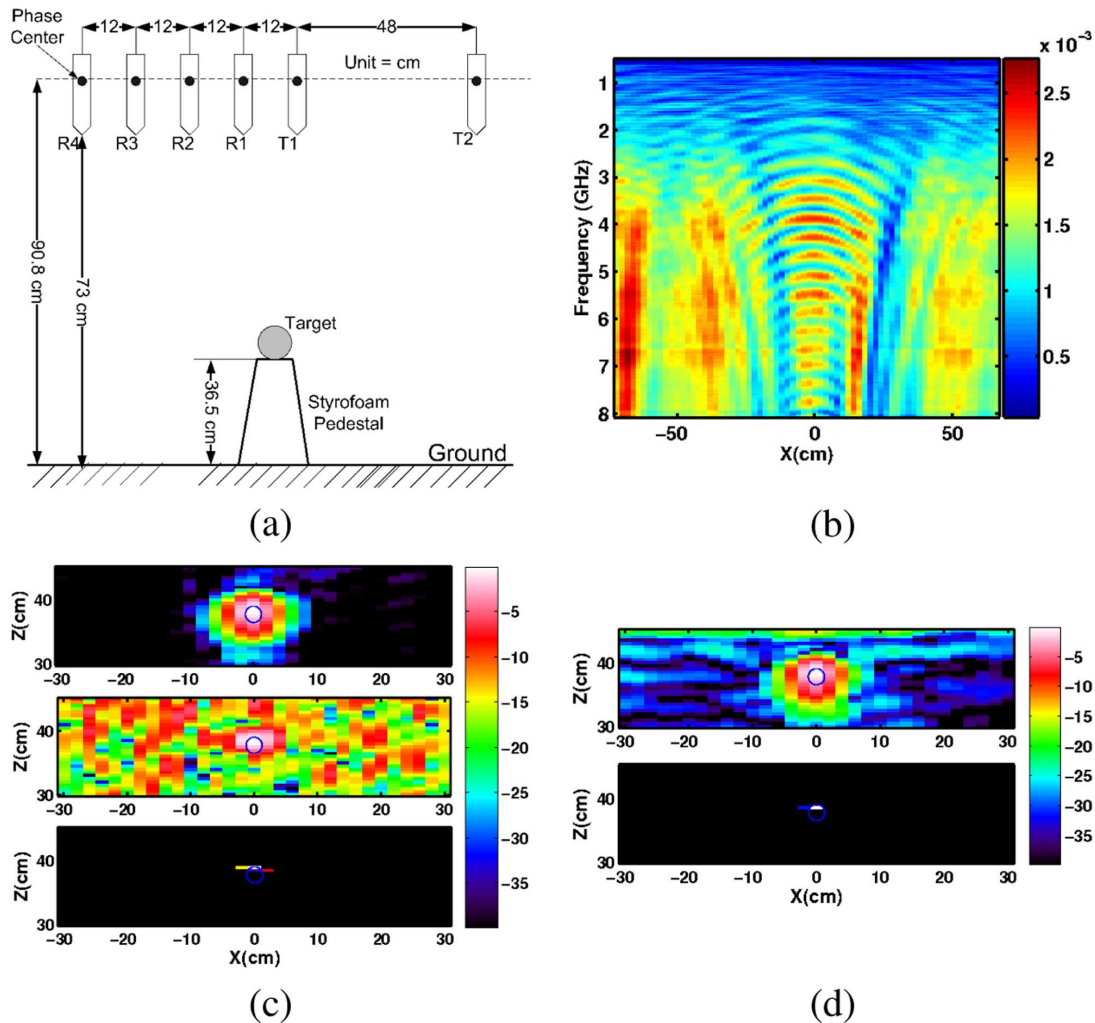


Fig. 7. (a) Experimental setup for GPR Imaging. (b) Magnitude of the space-frequency domain measured GPR Response of a 1'' metal sphere in air. (c) Top panel uses BP with all the space-frequency data, the middle and bottom panels are random frequency selection results generated by BP and the CS method. (d) Uniform frequency selection results: BP result in the top panel, CS in the bottom. Circles on the images indicate the true location and size of the sphere.

C. Increased Resolution

One of the important properties of the CS method is its ability to resolve targets spaced closer than the conventional range resolution of an SFCW GPR, defined as $\Delta R = c/(2L\Delta f)$, where Δf is the frequency step, L is the number of frequency steps, and c is the speed of the wave in the medium. To study this increased resolution property, a simulation is done with two point targets in air separated by 10 cm in height, at positions (0,45) cm and (0,55) cm. The GPR antenna scans the region $(-30, 30)$ cm along the x axis in 2 cm steps, and at each scan position collects data from 1 GHz to 3 GHz in $\Delta f = 20$ MHz increments, i.e., $N = 100$ frequency steps. For this simulated case, the range resolution is 7.5 cm.

Fig. 5(a) and (b) show the target space constructed using the BP and the CS methods, respectively. Although the CS method creates a much sparser target space, both methods are able to resolve the two targets. However, if the two targets are moved closer at (0,45) cm and (0,50) cm with a separation of 5 cm which is smaller than the resolution limit for the 2-GHz bandwidth, then Fig. 5(c) and (d) are obtained. While BP cannot resolve the two targets because they merge into a single peak,

the CS method resolves both targets at their correct positions. This is because the CS method doesn't perform a matched filtering operation, which would impose a resolution limit. Instead CS tries to explain the measurements using the least number of columns from its dictionary of measurements. The sparsity information about the image yields this increased resolution—a fact that has also been reported in other sparse signal reconstruction applications [46], [47].

D. Effect of Bandwidth

The bandwidth of the measured frequency spectrum is an important parameter in the SFCW GPRs. The CS method can generate sparse target space images even using small bandwidths, whereas standard imaging methods fail to produce a focused image. As a test of bandwidth, a sample target space containing two point targets at (10,37) and $(-10, 37)$ was imaged using bandwidths of 1, 3, and 7 GHz. One hundred trials were made and at each trial half of the frequency points for each bandwidth case were randomly measured. Noise (CWGN) was added to the measurements at an SNR of 10 dB. The mean of the generated target space images using BP and the CS method are shown in Fig. 6.

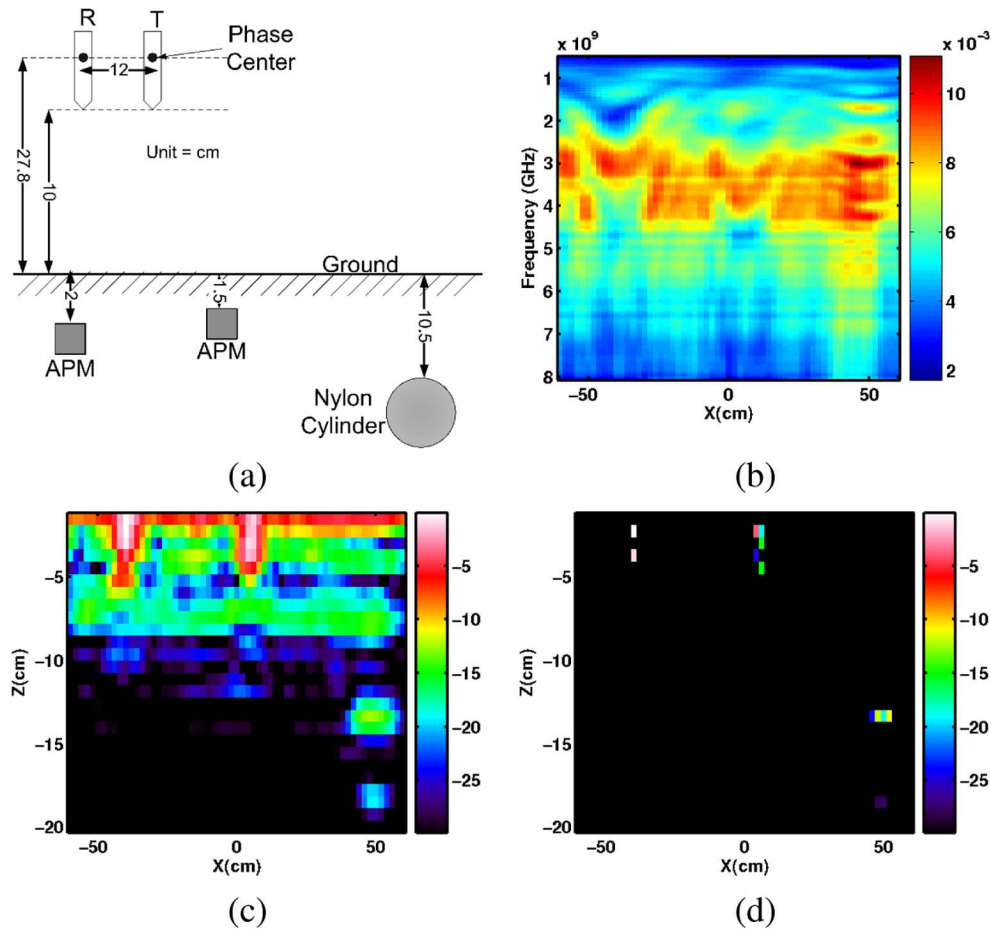


Fig. 8. (a) Experimental setup for buried target imaging. (b) Magnitude of the space-frequency measured GPR Response of 3 buried targets. (c) Target space image obtained with BP, and (d) with the CS method. The images in (c) and (d) are normalized to their own maxima and are shown on a 30-dB scale.

While increasing the bandwidth results in more focused images for BP, the CS method is able to reconstruct a very sparse image even for the low bandwidth case of 1 GHz.

E. Experimental Results

The CS algorithm was tested on experimental SFCW GPR data collected from a model mine field at the Georgia Institute of Technology [14], [48]. The GPR antenna [49] consists of eight bistatic pairs having varying transmitter-receiver distances, but for the results shown in this section only the data from the closest bistatic pair is used.

The GPR sweeps 379 equally spaced frequency points from 500 MHz to 8.06 GHz. For comparison reasons the full space-frequency domain data is measured and the random frequency selection results are created by only using the selected measurements. The data are publicly available online at <http://users.ece.gatech.edu/wrscott/> in Matlab format files. Two scenarios are tested.

1) *GPR Air Results*: The first experiment involves imaging a 1" diameter metal sphere held in the air at a height of 36.5 cm on a styrofoam support. The experimental setup is shown in Fig. 7(a). Both the GPR antenna and the target are in air, so the wave speed is $c = 3 \times 10^8$ m/s. The GPR scans the region in 2 cm increments at a constant height of 90.8 cm above ground level. The metal sphere is positioned at $x = 0$. The magnitude

of the raw frequency domain data measured over the target for a 2-D slice is shown in Fig. 7(b). These data contain reflections from the sphere as well as the ground.

If we had measured all of the space-frequency data and imaged the target space using BP, we would obtain the image in the top panel of Fig. 7(c). Instead of using all the space-frequency data, only 30 out of 379 frequency points are randomly selected at each aperture to be used for imaging. This gives more than a factor of 10 savings in data acquisition time if we only measure these frequencies. Applying BP to this randomly sampled data gives the image in the middle panel which is severely degraded compared to the top image. However, the CS method using the same randomly selected data set generates the bottom image shown in Fig. 7(c) which is a sparse image with much less clutter than BP. It consists of several point targets near the top of the metal sphere which seem to provide the necessary sparse fit to the measured data.

Another scheme for reducing the number of measurements would be uniform sampling over the bandwidth with larger frequency steps. BP and the CS method are applied to data which uses only 30 frequencies uniformly sampled over the full bandwidth at each scan position. The BP image shown in top panel of Fig. 7(d) is much more focused image than the one created using randomly selected data, however, it is still more cluttered than the full data BP or the CS-processed image shown in the

bottom panel of Fig. 7(d). The BP image varies significantly with a change in the subset of frequencies, but the CS method remains relatively stable.

2) *Buried Target Results*: In this experiment, two low-metal antipersonal mines and a nylon cylinder are buried in a sandbox at various depths. The targets are collinear, so the SFCW GPR can measure one line scan over the targets. The phase centers of the antennas are elevated 27.8 cm above the surface, and the transmitter-receiver distance is 12 cm. The spatial step size for the GPR scan is 2 cm. Fig. 8(a) shows the experimental setup and the actual target positions with their corresponding sizes. At each point 379 frequency points are measured. The magnitude of the measured raw frequency domain data is shown in Fig. 8(b).

The frequency domain BP result using all the space-frequency data is shown in Fig. 8(c). The three objects can be seen in the migrated BP image. The CS method uses 100 random frequency points instead of 379 and yields the target space image in Fig. 8(d) in which all the targets can be seen with less clutter in the image. Note that the reflections in Fig. 8(b) are mostly due to the reflection off the surface with only a minor part due to the mines. Both methods are pulling these small mine reflections out of the larger surface reflection.

V. CONCLUSION

A novel data acquisition and imaging algorithm for stepped frequency GPRs is demonstrated. The new method exploits the sparseness in the target space to reduce the data acquisition time significantly by decreasing the total number of measurements. An ℓ_1 minimization problem is solved to reconstruct the target space image from a small number of random space-frequency measurements. Noninteracting point-like structures are assumed, however, other target models or sparsity types might be used to improve the results. Initial results on simulated and experimental data show that extremely sparse images can be obtained with the proposed method in comparison to standard BP imaging algorithms with higher computational cost. The method is robust to noise, random spatial sampling and introduces increased resolution.

REFERENCES

- [1] D. J. Daniels, "Surface-penetrating radar," *Electron. Commun. Eng. J.*, vol. 8, pp. 165–182, 1996.
- [2] G. Grandjean, J. Gourry, and A. Bitri, "Evaluation of GPR techniques for civil-engineering applications: Study on a test site," *J. Appl. Geophys.*, vol. 45, no. 3, pp. 141–156, 2000.
- [3] P. Gader, M. Mystkowski, and Y. Zhao, "Landmine detection with ground penetrating radar using hidden Markov models," *IEEE Trans. Geosci. Remote Sens.*, vol. 39, pp. 1231–1244, 2001.
- [4] X. Feng and M. Sato, "Pre-stack migration applied to GPR for landmine detection," *Inverse Prob.*, vol. 20, pp. 99–115, 2004.
- [5] J. Groenenboom and A. Yarovsky, "Data processing and imaging in GPR system dedicated for landmine detection," *Subsurf. Sens. Technol. Appl.*, vol. 3, no. 4, pp. 387–402, 2002.
- [6] M. Sciotti, F. Colone, D. Pastina, and T. Bucciarelli, "GPR for archaeological investigations: Real performance assesment for different surface and subsurface conditions," in *Proc. IGARSS 03*, 2003, pp. 2266–2268.
- [7] S. Hubbard, C. Jinsong, K. Williams, Y. Rubin, and J. Peterson, "Environmental and agricultural applications of GPR," in *Proc. 3rd Int. Workshop on Adv. Ground Penetrating Radar*, 2005, pp. 45–49.
- [8] D. Daniels, *Ground Penetrating Radar*, 2nd ed. London, U.K.: The Inst. Elect. Eng. (IIE), 2004.
- [9] K. Iizuka, A. Freundorfer, K. Wu, H. Mori, H. Ogura, and V. Nguyen, "Step frequency radar," *J. Appl. Phys.*, vol. 56, no. 9, pp. 2572–2583, 1984.
- [10] N. Metje, P. Atkins, M. Brennan, D. Chapman, H. Lim, J. Machell, J. Muggleton, S. Pennock, J. Ratcliffe, M. Redfern, C. Rogers, A. Saul, Q. Shan, S. Swingler, and A. Thomas, "Mapping the underworld-state of the art review," *Tunnel. Underground Space Technol.*, vol. 22, pp. 568–586, 2007.
- [11] S. Lambot, E. Slob, I. van den Bosch, B. Stockbroeckx, and M. Vanclooster, "Modeling of ground-penetrating radar for accurate characterization of subsurface electric properties," *IEEE Trans. Geosci. Remote Sens.*, vol. 42, no. 11, pp. 2555–2568, 2004.
- [12] S. R. Axelsson, "Analysis of random step frequency radar and comparison with experiments," *IEEE Trans. Geosci. Remote Sens.*, vol. 45, no. 4, pp. 890–904, 2007.
- [13] A. Langman, "The design of hardware and signal processing for a stepped frequency continuous wave ground penetrating radar," Ph.D. dissertation, Univ. Cape Town, Cape Town, South Africa, 2002.
- [14] T. Counts, A. C. Gurbuz, W. R. Scott, Jr., J. H. McClellan, and K. Kangwook, "Multistatic ground-penetrating radar experiments," *IEEE Trans. Geosci. Remote Sens.*, vol. 45, no. 8, pp. 2544–2553, Aug. 2007.
- [15] O. Lopera, E. C. Slob, N. Milisavljevic, and S. Lambot, "Filtering soil surface and antenna effects from GPR data to enhance landmine detection," *IEEE Trans. Geosci. Remote Sens.*, vol. 45, no. 3, pp. 707–717, 2007.
- [16] F. Kong and T. L. By, "Performance of a GPR system which uses step frequency signals," *J. Appl. Geophys.*, vol. 33, pp. 15–26, 1995.
- [17] W. Steinway and C. Barrett, "Development status of a stepped-frequency ground penetrating radar," in *Proc. SPIE*, 1993, vol. 1942, pp. 34–43.
- [18] M. Bradley, T. Witten, R. McCummins, M. Crowe, S. Stewart, and M. Duncan, "Mine detection with a multi-channel stepped-frequency ground penetrating radar," in *Proc. SPIE*, 1999, vol. 3710, pp. 953–960.
- [19] S.-M. Oh, "Iterative space-time domain fast multiresolution SAR imaging algorithms," Ph.D. dissertation, Georgia Inst. Technol., Atlanta, GA, 2001.
- [20] J. Gazdag, "Wave equation migration with the phase shift method," *Geophys.*, vol. 43, pp. 1342–1351, 1978.
- [21] R. Stolt, "Migration by Fourier transform," *Geophys.*, vol. 43, pp. 23–48, 1978.
- [22] W. Schneider, "Integral formulation of migration in 2 and 3 dimensions," *Geophys.*, vol. 43, pp. 49–76, 1978.
- [23] D. Takhar, J. N. Laska, M. B. Wakin, M. F. Duarte, D. Baron, S. Sarvotham, K. F. Kelly, and R. G. Baraniuk, "A new compressive imaging camera architecture using optical-domain compression," in *Proc. Comp. Imag. IV at SPIE Electron. Imag.*, 2006, vol. 6065, pp. 43–52.
- [24] M. Lustig, D. Donoho, and J. Pauly, "Sparse MRI: The application of compressed sensing for rapid MR imaging," *Magn. Reson. Med.*, vol. 58, no. 6, pp. 1182–1195, Dec. 2007.
- [25] R. Baraniuk and P. Steeghs, "Compressive radar imaging," in *Proc. IEEE Radar Conf.*, 2007, pp. 128–133.
- [26] P. Bofill and M. Zibulevsky, "Underdetermined blind source separation using sparse representations," *Signal Process.*, vol. 81, pp. 2353–2362, 2001.
- [27] N. Aggarwal and W. C. Karl, "Line detection in images through regularized hough transform," *IEEE Trans. Image Process.*, vol. 15, pp. 582–590, 2006.
- [28] D. Donoho, "Compressed sensing," *IEEE Trans. Inf. Theory*, vol. 52, no. 4, pp. 1289–1306, 2006.
- [29] E. Candes, J. Romberg, and T. Tao, "Robust uncertainty principles: Exact signal reconstruction from highly incomplete frequency information," *IEEE Trans. Inf. Theory*, vol. 52, pp. 489–509, 2006.
- [30] R. Baraniuk, "Compressive sensing," *IEEE Signal Process. Mag.*, vol. 24, no. 4, pp. 118–121, Jul. 2007.
- [31] S. S. Chen, D. L. Donoho, and M. A. Saunders, "Atomic decomposition by basis pursuit," *SIAM J. Sci. Comput.*, vol. 20, pp. 33–61, 1999.
- [32] S. Mallat and Z. Zhang, "Matching pursuits with time-frequency dictionaries," *IEEE Trans. Signal Process.*, vol. 41, pp. 3397–3415, Dec. 1993.
- [33] S. R. Axelsson, "Beam characteristics of three-dimensional SAR in curved or random paths," *IEEE Trans. Geosci. Remote Sens.*, vol. 42, no. 10, pp. 2324–2334, 2004.
- [34] J. Ernst, H. Maurer, A. Green, and K. Holliger, "Full-waveform inversion of crosshole radar data based on 2-D finite-difference time-domain solutions of Maxwell's equations," *IEEE Trans. Geosci. Remote Sens.*, vol. 45, no. 9, pp. 2807–2828, 2007.
- [35] F. Soldovieri, J. Hugenschmidt, R. Persico, and G. Leone, "A linear inverse scattering algorithm for realistic GPR applications," *Near Surface Geophys.*, vol. 5, no. 1, pp. 29–41, 2007.

- [36] E. M. Johansson and J. E. Mast, "Three dimensional ground penetrating radar imaging using a synthetic aperture time-domain focusing," in *Proc. SPIE Conf. Adv. Microw. Millimeter Wave Detectors*, 1994, vol. 2275, pp. 205–214.
- [37] E. Candes and J. Romberg, "Sparsity and incoherence in compressive sampling," *Inverse Problems*, vol. 23, pp. 969–985, 2006.
- [38] E. Candès, J. Romberg, and T. Tao, "Stable signal recovery from incomplete and inaccurate measurements," *Comm. Pure Appl. Math.*, vol. 59, no. 8, pp. 1207–1223, 2006.
- [39] E. Candes and T. Tao, "The Dantzig selector: Statistical estimation when p is much larger than n ," *Ann. Statist.*, vol. 35, no. 6, pp. 2313–2351, 2007.
- [40] J. Haupt and R. Nowak, "Signal reconstruction from noisy random projections," *IEEE Trans. Inf. Theory*, vol. 52, no. 9, pp. 4036–4048, 2006.
- [41] D. Donoho, M. Elad, and V. Temlyakov, "Stable recovery of sparse overcomplete representations in the presence of noise," *IEEE Trans. Inf. Theory*, vol. 52, no. 1, pp. 6–18, 2006.
- [42] S. Boyd and L. Vandenberghe, *Convex Optimization*. Cambridge, U.K.: Cambridge Univ. Press, 2004.
- [43] M. Lobo, L. Vandenberghe, S. Boyd, and H. Le Bret, "Applications of second-order cone programming," *Linear Algebra Its Appl.*, no. 284, pp. 193–228, 1998.
- [44] P. Boufounos, M. Duarte, and R. Baraniuk, "Sparse signal reconstruction from noisy compressive measurements using cross validation," in *Proc. IEEE Workshop SSP*, Aug. 2007, pp. 299–303.
- [45] M. Grant and S. Boyd, CVX: Matlab Software for Disciplined Convex Programming (Web Page and Software) 2008 [Online]. Available: <http://stanford.edu/boyd/cvx>
- [46] D. Donoho, "Superresolution via sparsity constraints," *SIAM J. Math. Analysis*, vol. 23, no. 5, pp. 1309–1331, 1992.
- [47] D. Malioutov, M. Cetin, and A. Willsky, "A sparse signal reconstruction perspective for source localization with sensor arrays," *IEEE Trans. Signal Process.*, vol. 53, pp. 3010–3022, 2005.
- [48] A. C. Gurbuz, T. Counts, K. Kim, J. H. McClellan, and W. R. Scott, Jr., "Application of multistatic inversion algorithms to landmine detection," in *Proc. SPIE Detect. Remed. Technol. Mines and Minelike Targets XI*, May 2006, vol. 6217, 621724.
- [49] K. Kim, A. C. Gurbuz, J. H. McClellan, and W. R. Scott, Jr., "A multi-static ground-penetrating radar with an array of resistively loaded vee dipole antennas for landmine detection," in *Proc. SPIE Detect. Remed. Technol. Mines and Minelike Targets X*, Jun. 2005, vol. 5794, pp. 495–506.



Ali Cafer Gurbuz (M'08) received the B.S. degree from Bilkent University, Ankara, Turkey, in 2003 in electrical engineering, and the M.S. and Ph.D. degrees from the Georgia Institute of Technology (Georgia Tech), Atlanta, in 2005 and 2008, both in electrical and computer engineering, respectively.

From 2003 to 2008, he participated in multimodal landmine detection system research as a Graduate Research Assistant and from 2008 to 2009, as Postdoctoral Fellow, all with Georgia Tech. He is currently an Assistant Professor with TOBB University of Economics and Technology, Ankara, with the Department of Electric and Electronics Engineering. His research interests include compressive sensing, ground penetrating radar applications, fast feature detection techniques, and SAR imaging.



James H. McClellan (S'69–M'74–SM'79–F'85) received the B.S. degree in electrical engineering from Louisiana State University in 1969, and the M.S. and Ph.D. degrees from Rice University, Houston, TX, in 1972 and 1973, respectively.

From 1973 to 1982, he was a member of the Research Staff at Lincoln Laboratory and then a Professor with the Massachusetts Institute of Technology (MIT), Cambridge. From 1982 to 1987, he was with Schlumberger Well Services. Since 1987, he has been a Professor with the School of Electrical and Computer Engineering, Georgia Institute of Technology (Georgia Tech), Atlanta, where he presently holds the John and Marilu McCarty Chair. He is a coauthor of the texts *Number Theory in Digital Signal Processing*, *Computer Exercises for Signal Processing*, *DSP First: A Multimedia Approach*, and *Signal Processing First*, which received the McGraw-Hill Jacob Millman award for an outstanding innovative textbook in 2003.

Prof. McClellan received the W. Howard Ector Outstanding Teacher Award at Georgia Tech in 1998, and in 2001, the Education Award from the IEEE Signal Processing Society. In 1987, he received the Technical Achievement Award for work on FIR filter design, and in 1996, the Society Award, both from the IEEE Signal Processing Society. In 2004, he was a corecipient of the IEEE Jack S. Kilby Signal Processing medal. He is a member of Tau Beta Pi and Eta Kappa Nu.



Waymond R. Scott (S'81–M'82–SM'03–F'08) received the B.E.E., M.S.E.E., and Ph.D. degrees from the Georgia Institute of Technology (Georgia Tech), Atlanta, in 1980, 1982, and 1985, respectively.

In 1986, he joined the School of Electrical and Computer Engineering, Georgia Tech, as an Assistant Professor, where he was subsequently promoted to the rank of Professor. His research involves the interaction of electromagnetic and acoustic waves with materials. This research spans a broad range of topics, including the measurement of the properties of materials, experimental and numerical modeling, and systems for the detection of buried objects. Currently, his research is concentrated on investigating techniques for detecting objects buried in the earth. This work has many practical applications, for example, the detection of underground utilities, buried hazardous waste, buried structures, unexploded ordnance, and buried land mines.